


 Cite this: *New J. Chem.*, 2020, 44, 110

Copper(I) ionic complexes based on imidazo-[4,5-*f*][1,10]phenanthroline diimine chelating ligands: crystal structures, and photo- and electroluminescence properties†

 Anton V. Rozhkov,^{id}*^a Svetlana N. Eliseeva,^{id}^a Sergey V. Baykov,^{id}^a Lev E. Zelenkov,^{id}^a Dmitry O. Goriachiy^b and Ilya V. Taydakov^{id}^b

Four new ionic diimine Cu(I) complexes with general formula [Cu(POP)(NN)]BF₄ have been synthesized by convenient methods from readily available starting materials. All the complexes were characterized by a range of spectroscopic, electrochemical, and computational techniques and, in the cases of **1**, **2**, and **3**, by single crystal X-ray diffraction. The complexes are emissive in the solid state at ambient temperature and the emission maxima are located in the orange range. Furthermore, the suitability of these complexes for application in organic light-emitting diodes (OLEDs) has been demonstrated in a solution-processed device.

 Received 10th October 2019,
Accepted 25th November 2019

DOI: 10.1039/c9nj05109k

rsc.li/njc

Introduction

In recent times, luminescent Cu(I) complexes have been the object of intense studies for application in organic light emitting diodes (OLEDs).^{1–5} Cu(I) complexes possess significant advantages such as tunable phosphorescent emission bands, long excited state lifetimes, abundance of the metal in nature and easy mining, low cost, and environmental benignancy, which make them a tempting alternative to the commonly used triplet phosphorescent iridium complexes in electroluminescent device applications.⁶ Iridium and platinum complexes display strong spin–orbital coupling (SOC) leading to effective intersystem crossing from the lowest excited singlet to the lowest triplet state, which allows all injected excitons to be used for light generation in electroluminescent devices through the triplet harvesting effect.⁷ Yet another way to harvest excitons in OLEDs is to use temperature activated delayed fluorescence (TADF) emitters.^{8,9} Due to the small energy separation $\Delta E(S_1-T_1)$ between the first excited singlet state S_1 and the triplet state T_1 , the S_1 state can be thermally populated from the energetically lower lying T_1 state. In an electroluminescent device, this mechanism allows utilizing all injected excitons for light generation. Accordingly, the excitation is harvested and emitted, essentially, *via* the singlet S_1 state. As distinct from platinum and iridium complexes, copper(I)

complexes have smaller SOC constants, which can result in an increase in decay time and a decrease in triplet emission and can affect the OLED performance. Fortunately, copper complexes can show TADF with short radiative lifetimes at room temperature.^{10–13} These TADF copper complex-based OLEDs present an internal quantum efficiency of 100% by harvesting both singlet and triplet excitons. Copper(I) complexes with diimine ligands have been successfully used as TADF emitters.^{11,14,15} In particular, the imidazo[4,5-*f*][1,10]phenanthroline derivatives as ligands have been extensively utilized to prepare Cu(I) complexes with attractive luminescence features.^{16–19}

Herein, we describe the synthesis of a new series of cationic heteroleptic diimine–diphosphine copper(I) complexes with POP (bis[2-(diphenylphosphino)phenyl]ether) and 1,10-phenimidazole (**L1** = 2-(1*H*-imidazo[4,5-*f*][1,10]phenanthroline-2-yl)phenol, **L2** = 4-chloro-2-(1*H*-imidazo[4,5-*f*][1,10]phenanthroline-2-yl)phenol, **L3** = 4-bromo-2-(1*H*-imidazo[4,5-*f*][1,10]phenanthroline-2-yl)phenol, **L4** = 2-(1*H*-imidazo[4,5-*f*][1,10]phenanthroline-2-yl)-4-nitrophenol) ligands. These complexes demonstrated orange photoluminescence in the solid state at room temperature and were applied in solution-processed OLEDs using a host–guest system. We have found that the color of electroemission can be fine-tuned by varying the dopant concentration.

Results and discussion

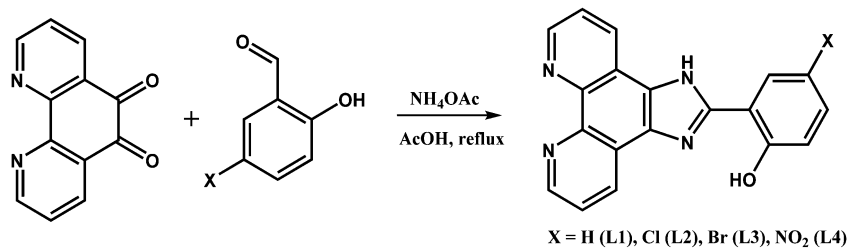
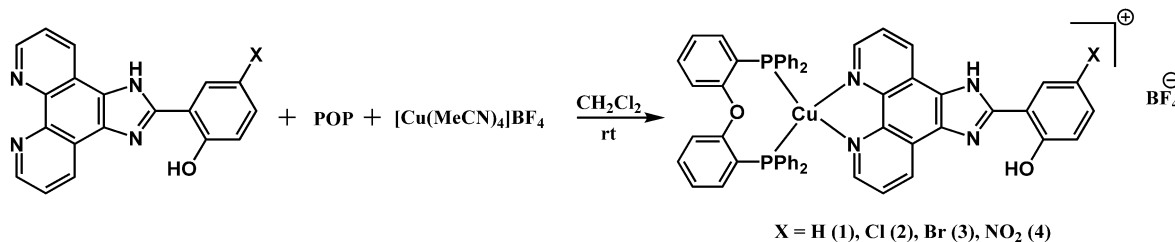
Synthetic procedures

The diimine N[^]N ligands **L1–L4** were prepared by condensation of 1,10-phenanthroline-5,6-dione with an appropriate aldehyde in the presence of ammonium acetate^{20–22} (Scheme 1).

^a Institute of Chemistry, Saint Petersburg State University, Universitetskaya Nab. 7/9, 199034 Saint Petersburg, Russian Federation. E-mail: iomcrozhkov@gmail.com

^b P. N. Lebedev Physical Institute of the Russian Academy of Science, Leninsky pr., 53, 119991 Moscow, Russian Federation

† Electronic supplementary information (ESI) available. CCDC 1941884, 1941885 and 1953636. For ESI and crystallographic data in CIF or other electronic format see DOI: 10.1039/c9nj05109k

Scheme 1 The synthetic route to the N^N ligands L1–L4.

Scheme 2 The synthetic route to the Cu(I) complexes.

The synthetic route to the Cu(I) complexes is shown in Scheme 2. Complexes 1–4 (X = H, Cl, Br, NO₂) were prepared by the conventional reaction of [Cu(CH₃CN)₄]BF₄ with 1 equiv. of the POP ligand and 1 equiv. of the appropriate N^N ligand in dichloromethane at room temperature.

The complexes were obtained in good yields as air stable, yellow crystalline solids soluble in the majority of organic solvents, including CHCl₃, CH₂Cl₂, MeOH, MeCN, DMF, and DMSO. The formation of the desired Cu(I) complexes was confirmed by ¹H, ¹³C, ³¹P NMR and FTIR spectroscopy, as well as high-resolution mass spectrometry (see the Experimental section).

Structure determination by single crystal X-ray diffraction

Single crystals suitable for X-ray determination were obtained by slow evaporation of the solvent from a DMSO solution (for complex 1) or by slow diffusion of pentane to a saturated solution of the complex in CH₂Cl₂ at ambient temperature (for complex 2). The structures obtained are presented in

Fig. 1 (complex 1), Fig. 2 (complex 2), and Fig. 3 (complex 3). Selected bond lengths and bond angles are given in Table 1.

All crystalized complexes display mononuclear structures. Complex 1 cocrystallized with one molecule of DMSO linked *via* the O1S···H3 hydrogen bond. Complex 2 cocrystallized with one molecule of dichloromethane. The Cl1S···Cl1 distance (3.36588(9) Å) is shorter than the corresponding sums of Bondi vdW radii (3.5 Å),²³ and the contact angle C1S–Cl1S–Cl1 (154.2208(9)°) does not significantly deviate from 160°. Both facts allow us to assign the observed intermolecular interaction to halogen bonding (Fig. S1, ESI†).²⁴ The Cu(I) center in all the complexes has a distorted tetrahedral geometry formed by two phosphorus atoms from the POP ligand and two nitrogen atoms from the diimine ligand. The Cu–N and Cu–P bond lengths are in the range of 2.05440(6)–2.081(2) Å and 2.2059(9)–2.2988(9) Å, respectively, which are consistent with the previously studied copper(I) complexes with the same or similar ligands.^{16,18,25–27} The P–Cu–P bite angle is 112.93(3)° in

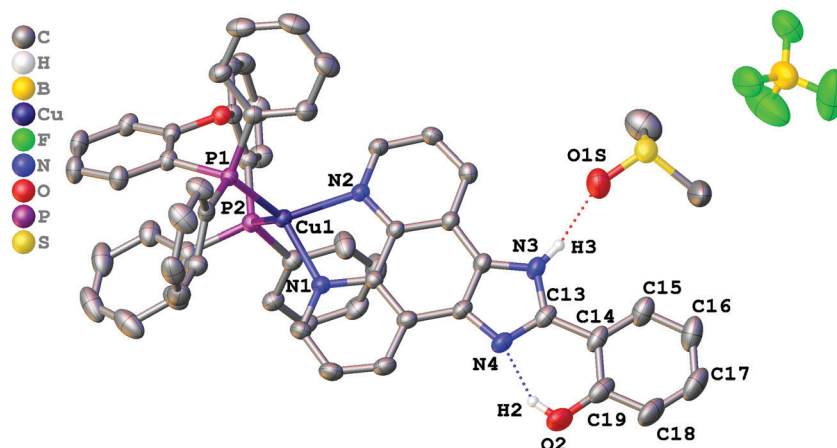


Fig. 1 Crystal structure of 1·DMSO with thermal ellipsoids shown at the 30% probability level. Most of the hydrogen atoms are omitted for clarity.

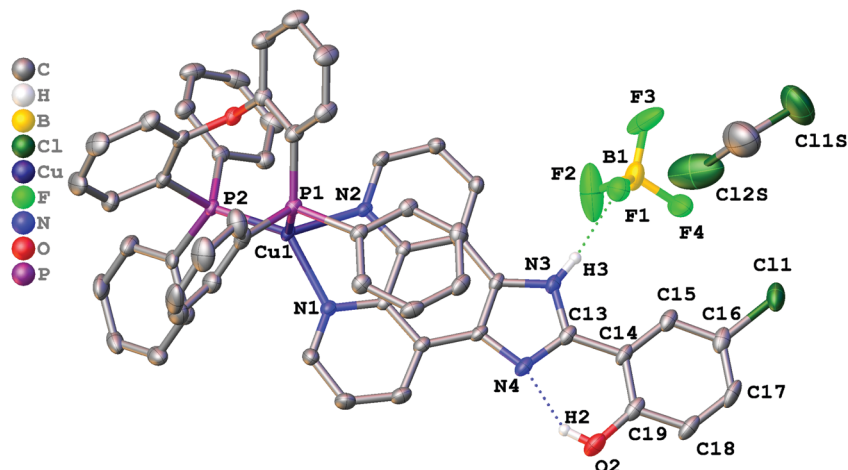


Fig. 2 Crystal structure of **2**·CH₂Cl₂ with thermal ellipsoids shown at the 30% probability level. Most of the hydrogen atoms are omitted for clarity.

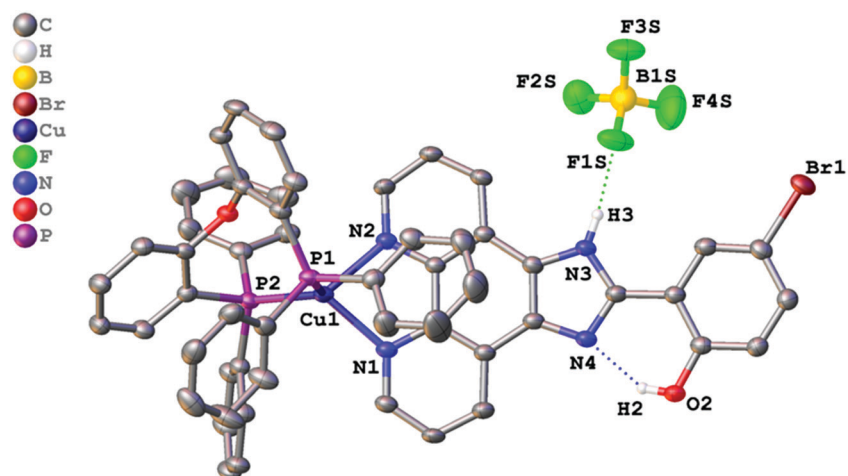


Fig. 3 Crystal structure of **3** with thermal ellipsoids shown at the 30% probability level. Most of the hydrogen atoms are omitted for clarity.

Table 1 Selected bond lengths (Å) and bond angles (°) in **1**·DMSO, **2**·CH₂Cl₂, and **3**

	1 ·DMSO	2 ·CH ₂ Cl ₂	3
Cu1–N1	2.059(2)	2.074(3)	2.068(2)
Cu1–N2	2.081(2)	2.054(3)	2.057(3)
Cu1–P1	2.2410(7)	2.2988(9)	2.2825(5)
Cu1–P2	2.2663(8)	2.2059(9)	2.2066(9)
N1–Cu1–N2	80.92(8)	81.18(9)	81.10(9)
P1–Cu1–P2	112.93(3)	114.69(3)	115.89(4)
N1–Cu1–P1	118.12(7)	98.33(7)	106.13(7)
N1–Cu1–P2	115.73(7)	132.53(8)	123.00(9)
N2–Cu1–P1	118.13(6)	101.57(7)	100.10(8)
N2–Cu1–P2	106.90(6)	121.06(7)	124.11(7)

1, 114.69(3)° in **2**, and 115.89(4)° in **3**. The angle between Cu–P1 and the mean plane of imidazo[4,5-*f*][1,10]phenanthroline in **2** (99.8875(12)°) is smaller than in **1** (128.27(4)°) due to the intramolecular $\pi \cdots \pi$ interaction between the POP phenyl group and the phenanthroline moiety of **L2**. The centroid distance is 3.33295(8) Å. Intramolecular O–H \cdots N hydrogen bonds are observed between the phenol –OH group and the other imidazole

nitrogen atom in all X-ray structures. It prevents the rotation of the phenyl group around the C13–C14 bond and leads to flattening of the diimine ligand and an increase in the degree of its conjugation. The dihedral angles between the phenol ring (C14–C19) and the mean plane of imidazo[4,5-*f*][1,10]phenanthroline are 2.98(11)° in **1**, 2.68540(8)° in **2**, and 0.30(11)° in **3**. Also, N–H \cdots F hydrogen bonds are observed in **2** and **3** between the imidazole –NH group and the BF₄[–] anion. In all obtained crystals, each molecule interacts with a neighbouring molecule through intermolecular $\pi \cdots \pi$ interactions (Fig. S2–S4, ESI[†]). $\pi \cdots \pi$ Overlapping formed through the stacking of imidazo[4,5-*f*][1,10]phenanthroline moieties with a $\pi \cdots \pi$ distance of 3.6118(17) Å in **1**, 3.4092(16) Å in **2**, and 3.6590(18) Å in **3**.

Thermal stability

Thermogravimetric analysis (TGA) was performed on samples of **1–4** powders under an argon atmosphere to investigate their stability characteristics. The TGA traces are presented in Fig. 4.

As shown by the TGA results, these complexes are thermally stable. The decomposition temperatures corresponding to a

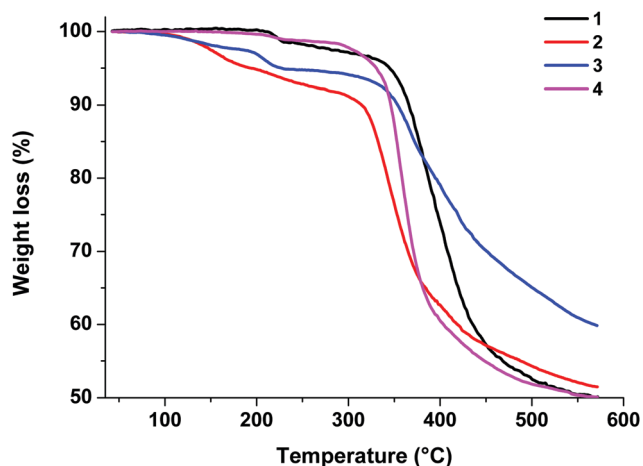


Fig. 4 TGA curves of complexes 1–4.

5% loss of weight are 344 °C for 1, 193 °C for 2, 227 °C for 3, and 330 °C for 4.

Photophysical properties

Absorption spectra. The absorption spectra of the complexes in anhydrous dichloromethane are shown in Fig. 5 and the photophysical data are summarized in Table 2. The intense absorption

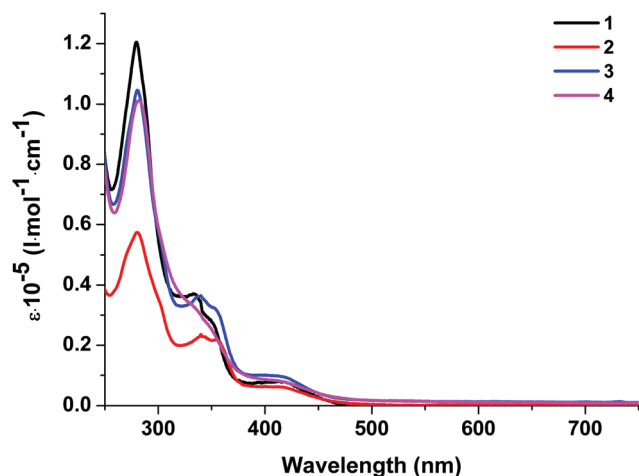


Fig. 5 Absorption spectra of complexes 1–4 in dichloromethane solution at room temperature.

bands in the range of 270–380 nm are assigned to the spin-allowed ligand centered (LC) transition ($\pi \rightarrow \pi^*$) of both the diimine ligand and the POP ligand, as well as the ligand-to-ligand charge-transfer (LLCT) transition. The weak low-energy bands in the range of 380 to 460 nm are attributed to the metal–ligand charge-transfer ($d\pi(\text{Cu}) \rightarrow \pi^*(\text{N}^{\wedge}\text{N} \text{ ligand})$) (MLCT) transition.^{16,17}

Emission spectra. All the complexes show no obvious emission in dichloromethane solution. The non-emissive behavior of complexes 1–4 in dichloromethane solution is assumed to arise from the active intramolecular motions (rotation and vibration). Complexes 1–4 demonstrate intense luminescence in the solid state at both 293 K and 77 K in air (Fig. 6 and Table 2).

At 293 K, the complexes show broad and structureless intense emission bands with maxima at 577 nm (1), 578 nm (2), 636 nm (3) and 594 nm (4), which could be assigned to the metal to ligand charge transfer (MLCT) character.^{27,29} At 77 K, complexes 1, 2, and 4 exhibit slightly lower energy emission with the peaks at 602, 596, and 564 nm, respectively. The considerable difference in emission between 293 K and 77 K indicates that the luminescence of these complexes in the solid state might originate from two different excited states in thermal equilibrium, that is, S_1 and T_1 . Small energy separations $\Delta E(S_1-T_1)$ of about 0.12 eV were observed for 1, 2, and 4. This behavior can be attributed to the TADF process.¹⁰ For complex 3 we did not detect a shift in the luminescence maxima upon a decrease in temperature to 77 K. The existence of Br in 3 led to spin-orbit coupling due to the heavy atom effect and we observed triplet emission at room temperature. The luminescence quantum yields of 1–4 at room temperature are in the range of 1.30–0.04% and the lifetimes are in the range of 1.5–4.2 μs (Table 2), which are close to those of other POP-based diimine copper complexes.^{16,27,30} It should be noted that replacement of H with Br at position 4 of the phenyl moiety in the $\text{N}^{\wedge}\text{N}$ ligand leads to a decrease in the quantum yield from 1.30 to 0.09% due to the heavy atom effect.³¹ Incorporation of an NO_2 group leads to a decrease in the quantum yield, too. Nitro group substituents that have acceptor properties may withdraw the π -electron density from the aromatic ring, thus increasing the ILCT and, accordingly, decreasing the MLCT processes.

Electrochemical properties

The electrochemical properties of complexes 1, 2, 3, and 4 were studied by cyclic voltammetry (Fig. 7).

Table 2 Photophysical data for the Cu(I) complexes

λ_{abs} , nm ($\epsilon \times 10^{-5}$ l mol ⁻¹ cm ⁻¹) (CH ₂ Cl ₂)	λ_{em} , nm		S_1 , ^a eV	T_1 , ^b eV	ΔE_{S-T} , eV	τ_{em} , μs	QY, %	ΔE_{g} , ^c eV	HOMO ^d /LUMO, ^e eV
	293 K	77 K							
1 280 (1.20), 334 (0.37), 350 sh (0.27), 420 (0.07)	577	602	2.39	2.27	0.12	4.2	1.30	2.75	-5.53/-2.78
2 280 (0.57), 340 (0.24), 356 (0.21), 420 (0.06)	578	596	2.37	2.25	0.12	3.9	0.85	2.75	-5.55/-2.80
3 280 (1.04), 339 (0.36), 353 (0.32), 420 (0.09)	636	636	2.19	—	—	1.5	0.09	2.79	-5.55/-2.76
4 281 (1.01), 338 sh (0.31), 419 (0.08)	594	622	2.31	2.19	0.12	1.9	0.04	2.74	-5.67/-2.93

^a Estimated from the high-energy flank at 50% of the emission maximum intensity measured at 298 K. ^b Estimated from the high-energy flank at 50% of the emission maximum intensity measured at 77 K. ^c Calculated from the absorption edge. ^d Estimated by cyclic voltammetry in DMF with SCE (4.74 eV) as the reference.²⁸ ^e Derived from the relation $\Delta E = \text{HOMO-LUMO}$.

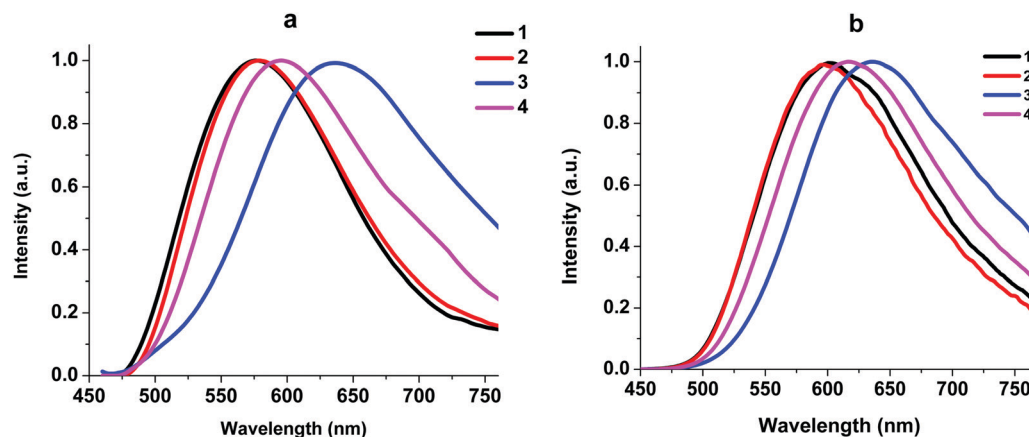


Fig. 6 Normalized emission spectra of neat powders of complexes **1–4** at 293 K (a) and 77 K (b). $\lambda_{\text{ex}} = 450$ nm.

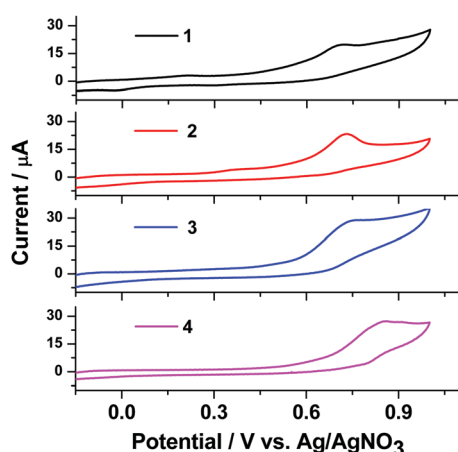


Fig. 7 Cyclic voltammograms of complexes **1–4** in DMF solution.

In cyclic voltammetry (CV) studies in the potential range from -0.2 to $+1.0$ V, complexes **1–4** show one oxidation peak at 0.72 – 0.86 V. Analysis of the CV dependence on the potential range at a scan rate of 50 mV s^{-1} shows that the peak potentials stabilize at 0.72 – 0.86 V for oxidation of complexes **1–4**, respectively. The oxidation potential of complexes **1**, **2**, **3**, and **4** in DMF solution is 0.72 , 0.74 , 0.74 and 0.86 V, respectively. In the CV of complex **4** we can see a wider oxidation peak at a higher potential (0.86 V) compared with the other complexes. All the Cu(I) complexes show an irreversible oxidation process, indicating a rapid decomposition of the Cu(II) species. Nevertheless, based on the start-of-oxidation potential, the highest occupied molecular orbital (HOMO) energy levels of these Cu(I) complexes can be calculated: -5.19 eV for **1**, -5.21 eV for **2**, -5.21 eV for **3** and -5.33 eV for **4**. The lowest unoccupied molecular orbitals (LUMOs) were determined from E_{HOMO} and the optical band gap ΔE_{g} values, which were obtained from the UV absorption edge as reported elsewhere.³² The LUMOs (-2.64 eV for **1**, -2.63 eV for **2**, -2.62 eV for **3** and -2.59 eV for **4**) of these complexes were obtained using the equation $E_{\text{LUMO}} = E_{\text{HOMO}} - \Delta E_{\text{g}}$. The corresponding data are summarized in Table 2 along with the optical band gap.

DFT calculations

In order to obtain insight into the optical spectroscopic results, TD-DFT (time-dependent DFT) calculations were performed. The computational methodology is described in detail in the Experimental section.

The frontier molecular orbitals (HOMO/LUMO) together with simulated absorption spectra of complex **1** as a representative example are shown in Fig. 8.

A good match is observed between the experimental spectrum and calculated bars. As expected, the HOMO of the complex is mainly localized over the metal center and phenyl and imidazole moieties of the phenanthroline-based ligand with little contribution of the triphenylphosphine coligand. On the other hand, the LUMO was mainly delocalized over the phenanthroline moiety of the diimine ligand (Fig. 8a). The main trends in the simulated spectra compare reasonably well with the corresponding solution spectra (Fig. 8b). The calculated lowest-energy absorption at 413 nm involves the HOMO \rightarrow LUMO transition, which can be assigned as the mixture of metal to ligand (Cu \rightarrow N^N) (MLCT), intra-ligand (ILCT), and ligand to ligand (POP \rightarrow N^N) (LLCT) charge transfer characters. At higher energies, *i.e.* 354 , 323 , 314 , 302 and 289 nm, MLCT and ILCT are the main characters with minor contribution of the LLCT character. At higher energies, *i.e.* 354 , 323 , 314 , 302 and 289 nm, IL, MLCT and ILCT are the main characters with minor contribution of the LLCT character. The calculated transitions with their assignments are summarized in Table 3.

Fig. S9–S12 (ESI[†]) depict the frontier molecular orbitals of complexes **1–4**.

Electroluminescence properties

Multilayer devices can be made by vacuum deposition, and commercial OLEDs are currently made using this process. However, vacuum thermal evaporation has the drawbacks of low material utilization rates, poor scalability, high capital cost, and difficulty in patterning. Solution processing, in principle, provides a low-cost approach to fabricate OLEDs.³³ To estimate the performance of the emitting compound upon electrical

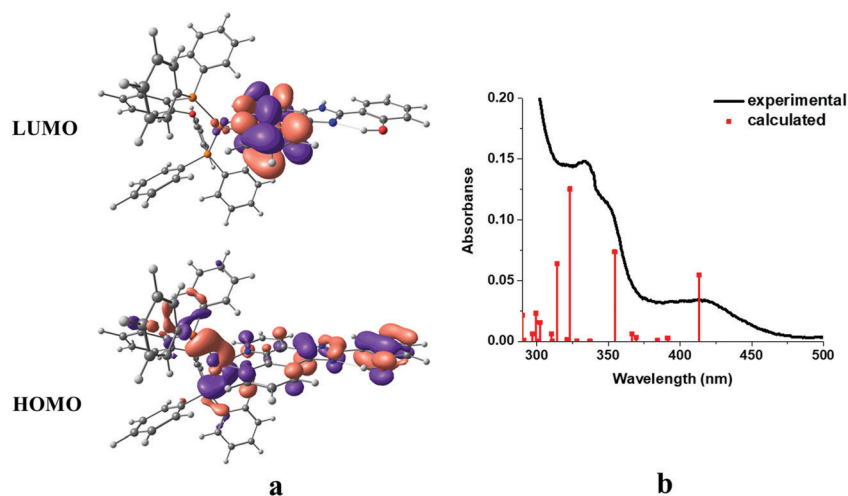


Fig. 8 Frontier orbitals (a) and simulated absorption spectra from TD-DFT calculations in dichloromethane (red bar) compared to solution absorption spectra (black line) of complex **1** (b).

Table 3 Calculated absorption spectra of complexes **1–4**

Model structure	λ (nm)	Oscillator strength	Transitions	Assignment
1	413	0.1750	HOMO \rightarrow LUMO	MLCT/ILCT/LLCT
	354	0.2353	HOMO-1 \rightarrow LUMO+1	MLCT/ILCT/LLCT
	323	0.4010	HOMO \rightarrow LUMO+2	MLCT/IL/LLCT
	314	0.2038	HOMO-1 \rightarrow LUMO+2	ILCT/LLCT
2	413	0.1811	HOMO \rightarrow LUMO	MLCT/LLCT
	352	0.3350	HOMO-1 \rightarrow LUMO+1	MLCT/IL
	329	0.1537	HOMO \rightarrow LUMO+2	LLCT
	322	0.2443	HOMO-1 \rightarrow LUMO+2	IL
	318	0.0706	HOMO-4 \rightarrow LUMO	ILCT
3	413	0.1796	HOMO \rightarrow LUMO	MLCT/ILCT/LLCT
	353	0.3269	HOMO-1 \rightarrow LUMO+1	MLCT/ILCT/LLCT
	329	0.1659	HOMO \rightarrow LUMO+2	IL/LLCT
	322	0.1399	HOMO-1 \rightarrow LUMO+2	IL/LLCT
	320	0.1374	HOMO-4 \rightarrow LUMO	ILCT
4	415	0.1561	HOMO \rightarrow LUMO+1	MLCT/LLCT
	368	0.0919	HOMO-1 \rightarrow LUMO	MLCT/ILCT
	336	0.1261	HOMO-3 \rightarrow LUMO	LLCT
	313	0.4852	HOMO-1 \rightarrow LUMO+3	IL

excitation, a solution-processed OLED test device was prepared with the following architecture: ITO/PEDOT:PSS/complex:CBP/TPBI/LiF/Al (Fig. 9). Water-soluble PEDOT:PSS was used as the hole-injection layer. A copper complex doped in the hole-transporting host (CBP (4,4'-bis(*N*-carbazolyl)-1,1'-biphenyl)) was spin-coated in CHCl₃ over PEDOT:PSS to form a light-emitting layer. TPBI (2,2',2''-(1,3,5-benzinetriyl)-tris(1-phenyl-1-*H*-benzimidazole)) was vacuum deposited and used as the electron-transporting and hole-blocking material.

Complex **1** was used for a test device to optimize the guest concentration due to its higher quantum yield among the rest of the complexes. The EL spectra are presented in Fig. 10a.

The EL spectra contain two types of emission bands: CBP emission (from 340 to 450 nm) and complex emission (from 450 to 800 nm). The CBP emission can be explained by incomplete energy transfer from host to guest molecules. In addition, we

observed a red shift of the complex emission maxima with increasing guest-host ratio (Fig. 10b). It is possibly due to increased stabilization of CT states as the concentration of highly polar dopant molecules increases. This behavior is very similar to the solvatochromic effect as a result of intermolecular solute-polar solvent interaction. The same phenomena were studied earlier for 2,3,5,6-tetrakis(3,6-diphenylcarbazol-9-yl)-1,4-dicyanobenzene as a TADF dopant in a CBP:4CzTPN-Ph blend as the emissive layer in OLEDs.³⁴ Additionally, the similarity of the peak shifting in various solvents and with different concentrations suggests that our complex suspended in a solid matrix of CBP undergoes an energy shift due to self-polarization.³⁵ When we increased the concentration of the complex in non-polar CBP, the distance between nearest complex molecules decreased, thereby increasing the local polarization field, which leads to the red shift. Furthermore,

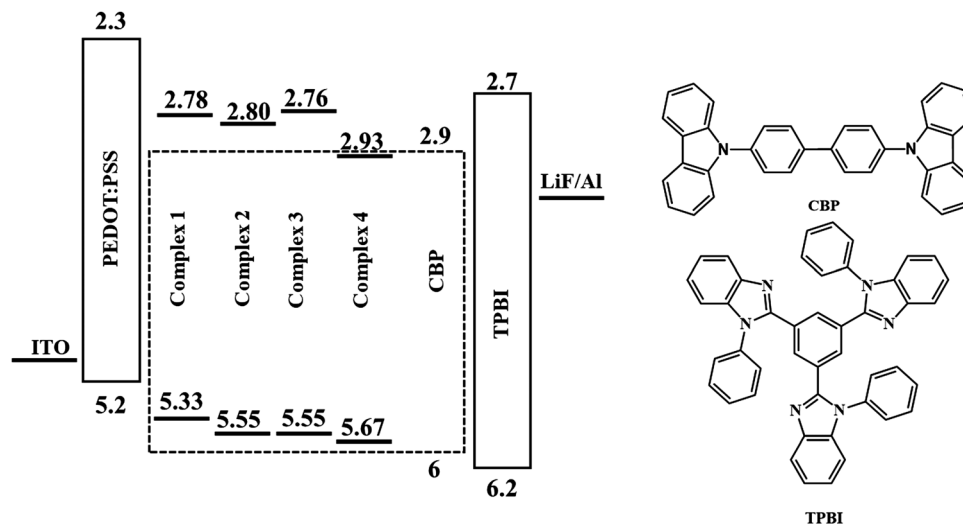


Fig. 9 Device architecture and molecular structures of the materials used in the OLEDs.

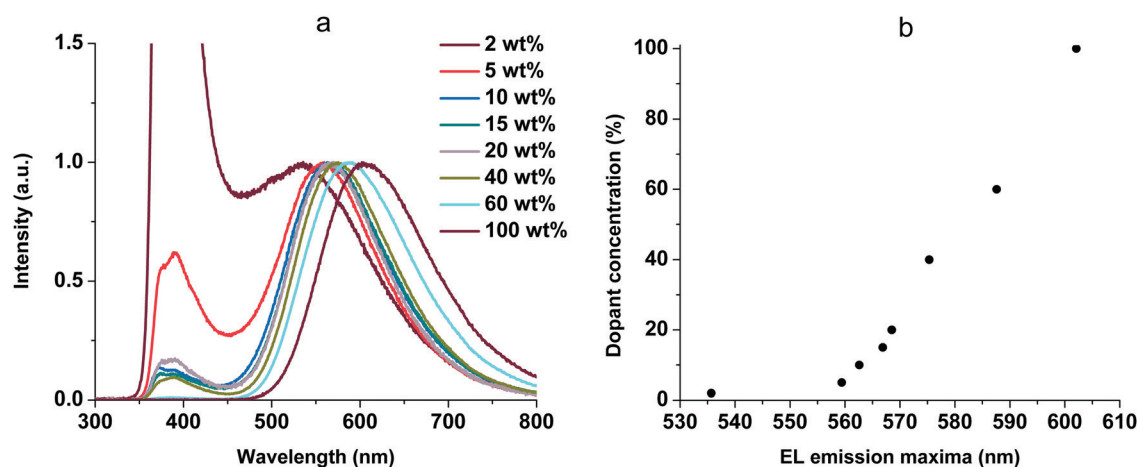


Fig. 10 EL spectra of the OLEDs (a) and EL emission maxima shift (b) at various doping concentrations of **1**.

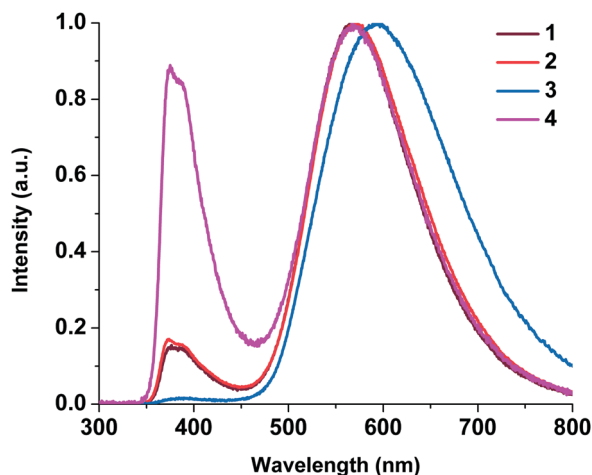


Fig. 11 EL spectra of ITO/PEDOT:PSS/complex (15 wt%):CBP/TPBI/LiF/Al.

with increasing dopant concentration the Dexter-type triplet-triplet energy transfer from the host to the dopant becomes more efficient.³⁶ The EL spectra of the host-free OLED (100 wt%, Fig. 10a) are identical to the PL spectra at 77 K (Fig. 6b), and the phosphorescence (triplet emission) process was observed. The best performance was achieved at 15 wt% of **1** and this concentration was used for all the complexes. The EL spectra are shown in Fig. 11. The EL spectra and luminance–voltage and current density–voltage characteristics of the OLED for **1** at different host–guest ratios are shown in Fig. S5 (ESI†).

Table 4 EL data for complexes **1–4**

Complex	$V_{\text{turn-on}}$ (V)	L_{max} (cd m^{-2})	η_c (cd A^{-1})	λ_{em} (nm)	CIE (x, y)
1	7	110	0.04 (10 V)	375, 386, 568	0.57, 0.39
2	7	50	0.02 (11 V)	375, 386, 568	0.57, 0.39
3	9	23	0.02 (10 V)	390, 595	0.60, 0.38
4	7	6	0.01 (7 V)	374, 387, 569	0.56, 0.39

The luminance–voltage and current density–voltage characteristics of the OLED are shown in Fig. S6 and S7 (ESI†). The EL data for complexes 1–4 are collected in Table 4.

Conclusions

In summary, four mononuclear cationic Cu(I) orange emitting complexes 1, 2, 3, and 4 bearing different substituents at position 4 of the phenol ring in the 1,10-phenimidazole ligand have been prepared and comprehensively characterized, including spectroscopic, electrochemical, and computational studies. The described complexes are suitable for applying in solution-processed OLEDs. Their electroluminescence properties are strongly affected by the dopant concentration. The optimal dopant concentration was estimated as 15 wt% for the best performance. A maximum luminance of 110 cd m⁻² was reached in the OLED based on complex 1. We believe that further optimization of the ligand structure and device architecture would allow enhanced OLED performance.

Experimental

Measurement and characterization

¹H, ¹³C, and ³¹P NMR spectra were measured on a Bruker 400 MHz WB Avance III spectrometer in DMSO-*d*₆ at ambient temperature; residual solvent signals were used as the internal standard. The ³¹P chemical shifts are referenced to 85% H₃PO₄. Melting points were measured on a Stuart SMP30 apparatus at a heating rate of 2 °C min⁻¹ in capillaries and were not corrected. Microanalyses (C, H, N) were carried out on a Euro EA3028-HT analyzer. Electrospray ionization mass spectra were obtained on a Bruker maXis spectrometer equipped with an electrospray ionization (ESI) source. The instrument was operated in positive ion mode using an *m/z* range of 50–3000. The capillary voltage of the ion source was set at ±70–150 V. The nebulizer gas pressure was 0.4 bar, and the drying gas flow was 4.0 L min⁻¹. The most intense peak is recorded in the isotopic pattern. Infrared spectra (4000–400 cm⁻¹) were recorded on a Shimadzu IRPrestige-21 instrument in KBr pellets. Ultraviolet-visible (UV-vis) absorption spectra were measured with a Shimadzu UV-1800 spectrophotometer. Emission spectra for solid-state samples at room temperature and at 77 K were measured on a Fluorolog 3 (Horiba Jobin Yvon) spectrofluorimeter. The photoluminescence quantum yield was defined as the number of photons emitted per photon absorbed by the system and was measured with an integrating sphere by a reported method.³⁷ TGA was performed on *ca.* 2 mg samples of 1–4 by using a Netzsch TG 209 F1 Libra thermal analyzer. The samples were dried under a vacuum at 50 °C before being heated from 40 to 600 °C at a heating rate of 10 K min⁻¹. A flow rate of 10 mL min⁻¹ of dry argon was used to purge the samples at all times.

Cyclic voltammetry

Electrochemical measurements were carried out with an Autolab PGSTAT30 (Eco Chemie, Netherlands) in a three-electrode cell

consisting of a working electrode (glassy carbon 0.07 cm²), a counter electrode (platinum wire) and a non-aqueous Ag/Ag⁺ reference electrode (Ag wire immersed in acetonitrile containing 0.1 M AgNO₃). All potentials in the text are referenced *vs.* the non-aqueous Ag/Ag⁺ electrode. The potential of the reference electrode was +0.07 V *vs.* saturated calomel electrode (SCE). Cyclic voltammetry measurements were performed at room temperature in argon purged anhydrous *N,N*-dimethylformamide solutions containing 1 × 10⁻³ M of a complex and 0.1 M of tetrabutylammonium tetrafluoroborate Bu₄NBF₄ (Aldrich) at a scan rate of 50 mV s⁻¹. The three-electrode electrochemical cell was sealed during the experiments. Before measurements, the solutions were bubbled with dry argon for 20 minutes.

Computational details

The DFT calculations were carried out with the B3LYP functional with inclusion of the CH₂Cl₂ solvent model (PCM) for studies of the electronic structures and the features of electronic transitions of the present complexes using the Gaussian-09 program package.³⁸ The starting structures for the geometry optimization procedure were taken from the experimental X-ray diffraction data and no symmetry restrictions were applied. The calculations were performed using the LANL2DZ effective core potentials and the appropriate contracted basis sets for the copper atoms and the standard 6-31G* basis sets for other atoms. Vibrational analysis at the same level was performed to confirm that all the optimized structures do not have imaginary frequencies.

OLED fabrication

1. Substrate preparation. ITO-coated glass substrates with 12 Ohm sq⁻¹ resistance were purchased from Lumtec Taiwan. The substrates were cleaned by sequential ultrasonication in alcohol 15% KOH solution, double distilled water, and isopropanol for 15 minutes each, followed by drying with a nitrogen flow. The substrates were additionally treated by UV/ozone in a UV-cleaning chamber (Ossila, UK) just before use.

2. Film deposition. In order to obtain films of PEDOT-PSS and complex:CBP we used a KW-4A spin coater from Chemat Technology (USA) operating in air. To form the PEDOT-PSS film (Lumtec LT-PS001), 200 μL of an aqueous solution was poured onto a resting ITO-substrate, then the rotation at 2000 rpm for 1 min was started. The 50 nm PEDOT-PSS films thus obtained were annealed at 100 °C for 30 min in an N₂ atmosphere.

Complex:CBP films were obtained by spin-coating on ITO/PEDOT-PSS from a 5 g l⁻¹ solution in chloroform by applying 100 μL of the solution onto a rotating substrate at 1500 rpm rotation for 1 min.

A 15 nm TPBi (Lumtec LT-E302) film was thermally deposited in a vacuum less than 10³ Pa from a quartz cuvette heated with a tantalum coil. Then 1 nm of LiF (Lumtec LT-E001) at a rate of 0.1 A s⁻¹ and 40 nm of aluminium at a rate of 0.2 nm s⁻¹ were thermally deposited through a mask to form four 12 mm² pixels.

3. Measurements. The electroluminescence spectra were obtained with an Ocean Optics Maya 2000 Pro CCD spectrometer sensitive within 200–1100 nm. The current–voltage characteristics

were obtained using two DT 838 digital multimeters. The luminance of the OLED samples was measured by a TKA-PKM luminance meter produced by TKA Scientific Instruments. The deposition rate was measured *in situ* by a Leybold Inficon IC-6000 deposition controller calibrated using a NT-MDT atomic force microscope of the Integra family.

Materials and reagents

[Cu(CH₃CN)₄]BF₄,³⁹ 1,10-phenanthro-5,6-dione,⁴⁰ 2-(1*H*-imidazo[4,5-*f*][1,10]phenanthrolin-2-yl)phenol (**L1**),²¹ 4-chloro-2-(1*H*-imidazo[4,5-*f*][1,10]phenanthrolin-2-yl)phenol (**L2**),²⁰ and 4-bromo-2-(1*H*-imidazo[4,5-*f*][1,10]phenanthrolin-2-yl)phenol (**L3**)²² were prepared according to the procedures reported in the literature. Bis[(2-diphenylphosphino)phenyl]ether (POP), poly-(3,4-ethylenedioxythiophene)polystyrene sulfonate (PEDOT:PSS), 4,4'-bis(*N*-carbazolyl)-1,1'-biphenyl (CBP), and 2,2',2''-(1,3,5-benzinetriyl)-tris(1-phenyl-1-*H*-benzimidazole) (TPBI) were obtained from commercial sources and used without further purification. All experiments with air and moisture sensitive intermediates and compounds were carried out under an inert atmosphere of dry argon using standard Schlenk techniques. The solvents were purified and dried by conventional methods.

Synthesis of 2-(1*H*-imidazo[4,5-*f*][1,10]phenanthrolin-2-yl)-4-nitrophenol (L4**).** 1,10-Phenanthro-5,6-dione (0.50 g, 2.38 mmol), 2-hydroxy-5-nitrobenzaldehyde (0.40 g, 2.38 mmol), and ammonium acetate (3.66 g, 47.57 mmol) were dissolved in glacial acetic acid (25 mL). The mixture was refluxed for 5 h with vigorous stirring using a magnetic stirrer. After the reaction mixture was cooled to room temperature, the solution was poured into cold water (200 mL) and cautiously neutralized with NH₃·H₂O until neutral. The precipitate was filtered off, washed with water and then acetone and vacuum dried at 50 °C to give the product as an orange solid (0.72 g, 85%). Mp: > 300 °C.

¹H NMR (400 MHz, DMSO-*d*₆) δ: 13.98 (br s, 2H), 8.99–8.93 (m, 3H), 8.70 (dd, *J* = 8.1, 1.5 Hz, 2H), 8.08 (dd, *J* = 9.1, 2.8 Hz, 1H), 7.72 (dd, *J* = 8.1, 4.3 Hz, 2H), 6.98 (d, *J* = 9.1 Hz, 1H). ¹³C NMR (101 MHz, DMSO-*d*₆) δ: 163.3, 148.8, 148.6, 144.2, 140.0, 130.0, 126.7, 123.6, 120.9, 122.5, 118.4, 113.4. HRMS (ESI⁺, MeOH): calcd for C₁₉H₁₁N₅O₃ [M + H]⁺ 358.0935; found 358.0936. IR (KBr, selected bands, cm⁻¹): 3068, 1594, 1481, 1411, 1342, 1301, 1126, 803, 738, 639.

General procedure for the synthesis of complexes 1–4. A mixture of [Cu(CH₃CN)₄]BF₄ (0.24 g, 0.76 mmol) and POP (0.41 g, 0.76 mmol) in CH₂Cl₂ (15 mL) was stirred for 1 h at room temperature. Then an N[^]N ligand (**L1–L4**) (0.76 mmol) was added and the mixture was stirred for 8 h. After solvent removal, the crude product was purified by crystallization.

Complex **1** was crystallized from CH₂Cl₂/pentane to yield the product as yellow crystals (0.66 g, 87%).

¹H NMR (400 MHz, DMSO-*d*₆) δ: 14.20 (s, 1H), 12.37 (s, 1H), 9.16 (d, *J* = 7.5 Hz, 2H), 8.87 (d, *J* = 4.3 Hz, 2H), 8.22 (d, *J* = 7.4 Hz, 1H), 7.94 (s, 2H), 7.47–7.42 (td, *J* = 7.9, 1.8 Hz, 3H), 7.30 (t, *J* = 7.4 Hz, 4H), 7.25–7.18 (m, 10H), 7.14–7.08 (m, 4H), 7.05–6.96 (m, 8H), 6.68 (m, 2H). ¹³C NMR (101 MHz, DMSO-*d*₆) δ: 158.4 (t, *J*_{CP} = 6.1 Hz), 157.6, 152.0, 148.3, 141.2, 134.3, 133.2 (t, *J*_{CP} = 8.1 Hz), 132.8, 132.4, 132.0, 131.0 (t, *J*_{CP} = 16.9 Hz),

130.6, 129.3 (t, *J*_{CP} = 4.4 Hz), 127.0, 125.7, 123.6 (t, *J*_{CP} = 14.6 Hz), 121.1, 120.0, 117.8, 113.3. ³¹P NMR (162 MHz, DMSO-*d*₆) δ: –11.64 (s). HRMS (ESI⁺, MeOH): calcd for C₅₅H₄₀CuN₄O₂P₂ [M]⁺ 913.1917; found 913.1915. IR (KBr, selected bands, cm⁻¹): 3538, 3228, 3054, 1710, 1586, 1574, 1564, 1480, 1462, 1436, 1407, 1359, 1258, 1213, 1186, 1096, 1070, 732, 694.

Complex **2** was crystallized from CH₂Cl₂/pentane to yield the product as yellow crystals (82%).

¹H NMR (400 MHz, DMSO-*d*₆) δ: 14.23 (s, 1H), 12.45 (s, 1H), 9.14 (d, *J* = 8.3 Hz, 2H), 8.87 (d, *J* = 4.7 Hz, 2H), 8.27 (d, *J* = 2.4 Hz, 1H), 8.01–7.89 (m, 2H), 7.48–7.43 (m, 3H), 7.31 (d, *J* = 7.4 Hz, 4H), 7.24–7.16 (m, 10H), 7.12 (m, 3H), 6.99 (m, 8H), 6.70–6.66 (m, 2H). ¹³C NMR (101 MHz, DMSO-*d*₆) δ: 158.4 (t, *J*_{CP} = 5.9 Hz), 156.3, 150.5, 148.4, 141.3, 134.3, 133.2 (t, *J*_{CP} = 8.0 Hz), 132.8, 132.0, 131.8, 131.0 (t, *J*_{CP} = 16.9 Hz), 130.6, 129.3 (t, *J*_{CP} = 4.5 Hz), 125.7, 123.6 (dd, *J*_{CP} = 16.1 Hz, 13.0 Hz), 121.1, 119.7, 114.8, 55.4. ³¹P NMR (162 MHz, DMSO-*d*₆) δ: –11.63 (s). HRMS (ESI⁺, MeOH): calcd for C₅₅H₃₉ClCuN₄O₂P₂ [M]⁺ 947.1527; found 947.1517. IR (KBr, selected bands, cm⁻¹): 3538, 3228, 3054, 1710, 1586, 1574, 1564, 1480, 1462, 1436, 1407, 1359, 1258, 1213, 1186, 1096, 1070, 732, 694.

Complex **3** was crystallized from CHCl₃/pentane to yield the product as orange crystals (78%).

¹H NMR (400 MHz, DMSO-*d*₆) δ: 13.43 (br s, 2H), 9.05 (d, *J* = 8.1 Hz, 2H), 8.77 (d, *J* = 4.6 Hz, 2H), 8.42 (s, 1H), 7.83 (m, 2H), 7.44 (m, 3H), 7.30 (t, *J* = 7.3 Hz, 4H), 7.24–7.16 (m, 10H), 7.09 (t, *J* = 7.5 Hz, 2H), 7.02–6.95 (m, 9H), 6.69–6.63 (m, 2H). ¹³C NMR (101 MHz, DMSO-*d*₆) δ: 158.4 (t, *J*_{CP} = 6.2 Hz), 156.9, 147.2, 140.8, 134.3, 133.2 (t, *J*_{CP} = 8.1 Hz), 132.8, 131.6, 131.2 (t, *J*_{CP} = 16.7 Hz), 130.5, 129.2 (t, *J*_{CP} = 4.5 Hz), 128.8, 125.6, 125.2, 123.7 (t, *J*_{CP} = 14.4 Hz), 121.1, 119.6, 110.5, 79.8, 79.6, 79.4, 79.1. ³¹P NMR (162 MHz, DMSO-*d*₆) δ: –11.88 (s). HRMS (ESI⁺, MeOH): calcd for C₅₅H₃₉BrCuN₄O₂P₂ [M]⁺ 991.1022; found 991.1022. IR (KBr, selected bands, cm⁻¹): 3540, 3070, 3055, 1587, 1574, 1479, 1462, 1435, 1398, 1257, 1211, 1161, 1094, 1055, 1000, 988, 873.

Complex **4** was crystallized from CH₂Cl₂/pentane to yield the product as orange crystals (81%).

¹H NMR (400 MHz, DMSO-*d*₆) δ: 14.02 (br s, 1H), 9.15 (s, 3H), 8.89 (s, 2H), 8.23 (s, 1H), 7.95 (s, 2H), 7.46 (t, *J* = 7.9 Hz, 3H), 7.31 (m, 4H), 7.25–7.16 (m, 8H), 7.11 (t, *J* = 7.5 Hz, 3H), 7.00 (m, 8H), 6.69 (m, 2H). ¹³C NMR (101 MHz, DMSO-*d*₆) δ: 158.4 (t, *J*_{C-P} = 5.8 Hz), 148.5, 141.4, 140.4, 134.3, 133.2 (t, *J*_{C-P} = 8.1 Hz), 132.9, 131.0 (t, *J*_{C-P} = 16.9 Hz), 130.6, 129.3, 125.7, 123.6 (t, *J*_{C-P} = 14.6 Hz), 121.1, 55.4. ³¹P NMR (162 MHz, DMSO-*d*₆) δ: –11.63 (s). HRMS (ESI⁺, MeOH): calcd for C₅₅H₃₉CuN₅O₄P₂ [M]⁺ 958.1768; found 958.1791. IR (KBr, selected bands, cm⁻¹): 3490, 3255, 3055, 1710, 1607, 1589, 1506, 1480, 1463, 1435, 1340, 1300, 1260, 1216, 1127, 1095, 1075, 1028, 998, 974.

X-Ray crystallography

The XRD experiments for complex **1** and **3** were performed on a SuperNova (Agilent Technologies/Oxford Diffraction) diffractometer, equipped with a dual microfocus Cu/Mo X-ray source and Atlas CCD detector, using monochromated Cu Kα (λ = 1.54184 Å) radiation. The XRD experiment for the **2** single crystal was

performed on an Xcalibur (Agilent Technologies/Oxford Diffraction) diffractometer using monochromated Mo K α ($\lambda = 0.71073$ Å) radiation. The temperature was kept at 100 K for 2 and 3, and 130 K for 1 because of possible crystal destruction at 100 K. The structures were solved by direct methods by means of the SHELX program⁴¹ incorporated in the OLEX2 program package.⁴² An empirical absorption correction was applied in the CrysAlisPro⁴³ software package using spherical harmonics implemented in the SCALE3 ABSPACK scaling algorithm. Supplementary crystallographic data for this paper have been deposited at the Cambridge Crystallographic Data Centre (CCDC numbers 1941884, 1941885, and 1953636).†

Conflicts of interest

There are no conflicts to declare.

Acknowledgements

This work was supported by RSF (17-73-10078). Physicochemical studies were performed at the Centre for Magnetic Resonance, Centre for X-ray Diffraction Studies, Thermogravimetric and Calorimetric Research Centre, Centre for Optical and Laser Materials Research, and Centre for Chemical Analysis and Materials Research (all belong to Saint Petersburg State University).

References

- 1 F. Dumur, *Org. Electron.*, 2015, **21**, 27–39.
- 2 C. Bizzarri, E. Spuling, D. M. Knoll, D. Volz and S. Bräse, *Coord. Chem. Rev.*, 2018, **373**, 49–82.
- 3 R. Hamze, J. L. Peltier, D. Sylvinson, M. Jung, J. Cardenas, R. Haiges, M. Soleilhavoup, R. Jazzar, P. I. Djurovich, G. Bertrand and M. E. Thompson, *Science*, 2019, **363**, 601.
- 4 M. Xie, C. Han, Q. Liang, J. Zhang, G. Xie and H. Xu, *Sci. Adv.*, 2019, **5**, eaav9857.
- 5 M. W. Mara, K. A. Fransted and L. X. Chen, *Coord. Chem. Rev.*, 2015, **282–283**, 2–18.
- 6 D. Volz, M. Wallesch, C. Fléchon, M. Danz, A. Verma, J. M. Navarro, D. M. Zink, S. Bräse and T. Baumann, *Green Chem.*, 2015, **17**, 1988–2011.
- 7 H. Yersin, A. F. Rausch, R. Czerwieńiec, T. Hofbeck and T. Fischer, *Coord. Chem. Rev.*, 2011, **255**, 2622–2652.
- 8 H. Yersin, R. Czerwieńiec, M. Z. Shafikov and A. F. Suleymanova, *ChemPhysChem*, 2017, **18**, 3508–3535.
- 9 Z. Yang, Z. Mao, Z. Xie, Y. Zhang, S. Liu, J. Zhao, J. Xu, Z. Chi and M. P. Aldred, *Chem. Soc. Rev.*, 2017, **46**, 915–1016.
- 10 R. Czerwieńiec, M. J. Leitzl, H. H. H. Homeier and H. Yersin, *Coord. Chem. Rev.*, 2016, **325**, 2–28.
- 11 Y. Zhang, M. Schulz, M. Wächtler, M. Karnahl and B. Dietzek, *Coord. Chem. Rev.*, 2018, **356**, 127–146.
- 12 C. Bizzarri, F. Hundemer, J. Busch and S. Bräse, *Polyhedron*, 2018, **140**, 51–66.
- 13 L. Bergmann, G. J. Hedley, T. Baumann, S. Bräse and I. D. W. Samuel, *Sci. Adv.*, 2016, **2**, e1500889.
- 14 F. Zhang, Y. Guan, X. Chen, S. Wang, D. Liang, Y. Feng, S. Chen, S. Li, Z. Li, F. Zhang, C. Lu, G. Cao and B. Zhai, *Inorg. Chem.*, 2017, **56**, 3742–3753.
- 15 F. Brunner, A. Babaei, A. Pertegás, J. M. Junquera-Hernández, A. Prescimone, E. C. Constable, H. J. Bolink, M. Sessolo, E. Ortí and C. E. Housecroft, *Dalton Trans.*, 2019, **48**, 446–460.
- 16 R. Liu, M.-M. Huang, X.-X. Yao, H.-H. Li, F.-L. Yang and X.-L. Li, *Inorg. Chim. Acta*, 2015, **434**, 172–180.
- 17 M.-M. Huang, Y.-M. Guo, Y. Shi, L. Zhao, Y.-W. Niu, Y. Shi and X.-L. Li, *Inorg. Chim. Acta*, 2017, **457**, 107–115.
- 18 X. Liu, R. Li, L. Ma, X. Feng and Y. Ding, *New J. Chem.*, 2016, **40**, 619–625.
- 19 C. Yi, S. Xu, J. Wang, F. Zhao, H. Xia and Y. Wang, *Eur. J. Inorg. Chem.*, 2016, 4885–4890.
- 20 N. M. Gabra, B. Mustafa, Y. P. Kumar, C. Shobha Devi, M. Shilpa, K. L. Reddy and S. Satyanarayana, *Med. Chem. Res.*, 2014, **23**, 224–235.
- 21 Z.-B. Cai, L.-F. Liu, Y.-Q. Hong and M. Zhou, *J. Coord. Chem.*, 2013, **66**, 2388–2397.
- 22 M. Gomleksiz, B. Erdem and C. Alkan, *S. Afr. J. Chem.*, 2013, **66**, 107–112.
- 23 A. Bondi, *J. Phys. Chem.*, 1966, **70**, 3006–3007.
- 24 G. Cavallo, P. Metrangolo, R. Milani, T. Pilati, A. Priimagi, G. Resnati and G. Terraneo, *Chem. Rev.*, 2016, **116**, 2478–2601.
- 25 Y. Shi, X. Liu, Y. Shan, X. Zhang, W. Kong, Y. Lu, Z. Tan and X.-L. Li, *Dalton Trans.*, 2019, **48**, 2430–2441.
- 26 X. Liu, Y. Shan, J. Xu, X. Zhang, S. Shang and X.-L. Li, *Polyhedron*, 2019, **164**, 152–158.
- 27 L. Shi and B. Li, *Eur. J. Inorg. Chem.*, 2009, 2294–2302.
- 28 C. Q. Ma, L. Q. Zhang, J. H. Zhou, X. S. Wang, B. W. Zhang, Y. Cao, P. Bugnon, M. Schaer, F. Nüesch, D. Q. Zhang and Y. Qiu, *J. Mater. Chem.*, 2002, **12**, 3481–3486.
- 29 D. G. Cuttall, S.-M. Kuang, P. E. Fanwick, D. R. McMillin and R. A. Walton, *J. Am. Chem. Soc.*, 2002, **124**, 6–7.
- 30 S.-X. Xu, J.-L. Wang, F. Zhao, H.-Y. Xia and Y.-B. Wang, *Transition Met. Chem.*, 2015, **40**, 723–732.
- 31 K. N. Solov'ev and E. A. Borisevich, *Phys.-Usp.*, 2005, **48**, 231–253.
- 32 J. Chen, T. Teng, J.-Y. Wang, L. Kang, X.-L. Chen, L.-J. Xu, R. Yu and C.-Z. Lu, *Eur. J. Inorg. Chem.*, 2016, 3036–3041.
- 33 P.-A. Will and S. Reineke, in *Handbook of Organic Materials for Electronic and Photonic Devices*, ed. O. Ostroverkhova, Woodhead Publishing, 2nd edn, 2019, pp. 695–726.
- 34 Y. R. Cho, S. J. Cha and M. C. Suh, *Synth. Met.*, 2015, **209**, 47–54.
- 35 V. Bulović, A. Shoustikov, M. A. Baldo, E. Bose, V. G. Kozlov, M. E. Thompson and S. R. Forrest, *Chem. Phys. Lett.*, 1998, **287**, 455–460.
- 36 W. S. Jeon, T. J. Park, S. Y. Kim, R. Pode, J. Jang and J. H. Kwon, *Org. Electron.*, 2009, **10**, 240–246.
- 37 C. Würth, M. Grabolle, J. Pauli, M. Spieles and U. Resch-Genger, *Nat. Protoc.*, 2013, **8**, 1535.
- 38 M. J. Frisch, G. W. Trucks, H. B. Schlegel, G. E. Scuseria, M. A. Robb, J. R. Cheeseman, G. Scalmani, V. Barone, B. Mennucci, G. A. Petersson, H. Nakatsuji, M. Caricato,

- X. Li, H. P. Hratchian, A. F. Izmaylov, J. Bloino, G. Zheng, J. L. Sonnenberg, M. Hada, M. Ehara, K. Toyota, R. Fukuda, J. Hasegawa, M. Ishida, T. Nakajima, Y. Honda, O. Kitao, H. Nakai, T. Vreven, J. A. Montgomery, Jr., J. E. Peralta, F. Ogliaro, M. Bearpark, J. J. Heyd, E. Brothers, K. N. Kudin, V. N. Staroverov, T. Keith, R. Kobayashi, J. Normand, K. Raghavachari, A. Rendell, J. C. Burant, S. S. Iyengar, J. Tomasi, M. Cossi, N. Rega, J. M. Millam, M. Klene, J. E. Knox, J. B. Cross, V. Bakken, C. Adamo, J. Jaramillo, R. Gomperts, R. E. Stratmann, O. Yazyev, A. J. Austin, R. Cammi, C. Pomelli, J. W. Ochterski, R. L. Martin, K. Morokuma, V. G. Zakrzewski, G. A. Voth, P. Salvador, J. J. Dannenberg, S. Dapprich, A. D. Daniels, O. Farkas, J. B. Foresman, J. V. Ortiz and D. J. Fox, *Gaussian 09, Revision C.01*, Gaussian, Inc., Wallingford, CT, 2009.
- 39 N. Busschaert, C. Caltagirone, W. Van Rossom and P. A. Gale, *Chem. Rev.*, 2015, **115**, 8038–8155.
- 40 J. R. Hickson, S. J. Horsewill, C. Bamforth, J. McGuire, C. Wilson, S. Sproules and J. H. Farnaby, *Dalton Trans.*, 2018, **47**, 10692–10701.
- 41 G. Sheldrick, *Acta Crystallogr., Sect. A: Found. Adv.*, 2015, **71**, 3–8.
- 42 O. V. Dolomanov, L. J. Bourhis, R. J. Gildea, J. A. K. Howard and H. Puschmann, *J. Appl. Crystallogr.*, 2009, **42**, 339–341.
- 43 CrysAlisPro, Version 1.171.136.120, Agilent Technologies Ltd, release 127-106-2012.